CrossMark

Discovery of a Variable Multiphase Outflow in the X-Ray-emitting Tidal Disruption Event ASASSN-20qc

P. Kosec[1] , D. Pasham[1], E. Kara[1] , and F. Tombesi[2,3,4,5,6]
[1] MIT Kavli Institute for Astrophysics and Space Research, Massachusetts Institute of Technology, Cambridge, MA 02139, USA; pkosec@mit.edu
[2] Physics Department, Tor Vergata University of Rome, Via della Ricerca Scientifica 1, I-00133 Rome, Italy
[3] INAF Astronomical Observatory of Rome, Via Frascati 33, I-00040 Monte Porzio Catone, Italy
[4] INFN—Rome Tor Vergata, Via della Ricerca Scientifica 1, I-00133 Rome, Italy
[5] Department of Astronomy, University of Maryland, College Park, MD 20742, USA
[6] NASA Goddard Space Flight Center, Code 662, Greenbelt, MD 20771, USA

Abstract

Tidal disruption events (TDEs) are exotic transients that can lead to temporary super-Eddington accretion onto a supermassive black hole. Such an accretion mode is naturally expected to result in powerful outflows of ionized matter. However, to date such an outflow has only been directly detected in the X-ray band in a single TDE, ASASSN-14li. This outflow has a low velocity of just a few $100 \, \mathrm{km \, s^{-1}}$, although there is also evidence for a second, ultrafast phase. Here we present the detection of a low-velocity outflow in a second TDE, ASASSN-20qc. The high-resolution X-ray spectrum reveals an array of narrow absorption lines, each blueshifted by a few $100 \, \mathrm{km \, s^{-1}}$, which cannot be described by a single photoionization phase. For the first time, we confirm the multiphase nature of a TDE outflow, with at least two phases and two distinct velocity components. One highly ionized phase is outflowing at $910^{+90}_{-80} \, \mathrm{km \, s^{-1}}$, while a lower ionization component is blueshifted by $400^{+100}_{-120} \, \mathrm{km \, s^{-1}}$. We perform a time-resolved analysis of the X-ray spectrum and detect that, surprisingly, the ionization parameter of the mildly ionized absorber strongly varies over the course of a single 60 ks observation, indicating that its distance from the black hole may be as low as 400 gravitational radii. We discuss these findings in the context of TDEs and compare this newly detected outflow with that of ASASSN-14li.

1. Introduction

A tidal disruption event (TDE) is an exotic transient during which a star is disrupted as it ventures too close to a supermassive black hole (Rees 1988). A significant fraction of the star's mass is accreted, which can lead to temporary super-Eddington accretion rates onto the black hole. In recent years, dozens of TDEs were discovered, in the optical band (van Velzen et al. 2021; Hammerstein et al. 2023) as well as in the X-rays (Sazonov et al. 2021). For recent reviews, see Gezari (2021) and Saxton et al. (2020). These events open a unique window into the lives of supermassive black holes in galaxies, the majority of which are inactive and thus challenging to study through other means.

The violent, supercritical nature of this phenomenon is naturally expected to result in massive and high-velocity ($\sim 0.1c$) outflows of ionized matter from the accretion flow (Shakura & Sunyaev 1973). Such outflows are observed in simulations of supercritical flows (Ohsuga et al. 2009; Ohsuga & Mineshige 2011; Takeuchi et al. 2013) and were observationally confirmed in other super-Eddington or highly accreting systems such as ultraluminous X-ray sources (Pinto et al. 2016; Kosec et al. 2018; Pinto et al. 2021) and active galactic nuclei (AGN; e.g., Pounds et al. 2003; Tombesi et al. 2010). Physical models and simulations of super-Eddington accretion predict the existence of a geometrically and optically thick accretion flow (Ohsuga et al. 2005). The appearance and

emission pattern of such a flow is thus inherently strongly nonisotropic. This is a possible explanation for why some TDEs are primarily bright in the optical band, and some others instead in the X-rays (Dai et al. 2018). It is thus of great importance to detect and understand the properties of outflows launched by TDEs, as they may strongly modify the inner accretion flow properties.

Observational evidence for these outflows in TDEs has however been sparse so far. The first TDE with a confirmed outflow in the X-rays was the nearby event ASASSN-14li (Miller et al. 2015). The properties of this detected outflow phase are rather puzzling—Miller et al. (2015) found that the outflow had a low systematic velocity of just 200–$300 \, \mathrm{km \, s^{-1}}$, in contrast with the expected velocities in excess of 5% of the speed of the light, as seen in the other supercritical systems mentioned above. Kara et al. (2018) later found evidence for a second, high-velocity component of the outflow at $\sim 0.2c$ in ASASSN-14li, and Kara et al. (2016) found evidence for a high-velocity outflow originating from the inner accretion flow of the jetted TDE Swift J164457 through X-ray reverberation. However, it is unclear what is the driving mechanism of any of these X-ray outflows, and what is their relationship with the TDE. Clearly, the detection of outflows in further TDEs is necessary to understand their nature, physics, and impact on the accretion flow as well as the black hole surroundings. Outside the X-ray band, an outflow was detected in the TDE AT2019qiz via its optical line shape evolution (Nicholl et al. 2020), and likely corresponds to the expanding TDE photosphere, which is the dominant source of the optical and UV radiation.

Here we study ASASSN-20qc ($z = 0.056$; Stanek 2020; Hinkle 2022), previously a low-luminosity AGN, which turned into an X-ray bright TDE (D. Pasham et al. 2023, submitted), sharing a number of similarities with ASASSN-14li. ASASSN-20qc was the target of a large multiwavelength campaign in 2021. It was detected in the X-rays by the eROSITA survey and observed by the XMM-Newton and NICER observatories. Its X-ray spectrum reveals a soft X-ray continuum, which can be broadly described by a disk blackbody with a temperature of ~90 eV. Similar to ASASSN-14li (Kara et al. 2018), the spectrum appears to show a significant broad dip around the Wien tail. This feature, if modeled as an absorption line, suggests an outflow velocity of $0.3c$. We refer to D. Pasham et al. (2023, submitted) for a detailed analysis of this ultrafast outflow (UFO) component.

In this paper, we instead focus on the high-resolution XMM-Newton RGS spectra of ASASSN-20qc, which reveal an array of absorption lines, similar to those found in ASASSN-14li. ASASSN-20qc is only the second TDE to exhibit such narrow lines. The structure of this paper is as follows. Our data preparation and reduction is summarized in Section 2. The spectral modeling and the results are described in Section 3. We discuss the results and their implications in Section 4 and conclude in Section 5.

2. Data Reduction and Preparation

XMM-Newton (Jansen et al. 2001) observed ASASSN-20qc six times to date. Here we analyze observation 0852600301, the only observation which occurred when the source was in a high-flux state, allowing us to use the high-spectral resolution data from the Reflection Grating Spectrometer (RGS). During the remaining five XMM-Newton observations, ASASSN-20qc reached an order of magnitude lower count rates. Observation 0852600301 occurred on 2021 March 14 and had a duration of ≈60 ks. The data were downloaded from the XSA archive and reduced using a standard pipeline with SAS v20, CALDB as of 2022 April. We use data from RGS (den Herder et al. 2001) and from the European Photon Imaging Camera (EPIC)-pn (Strüder et al. 2001).

The RGS data were reduced following standard routines using the RGSPROC procedure, centering the extraction regions on the coordinates of ASASSN-20qc. We filtered for any periods of high background, but the RGS detectors were not significantly affected by any major flares, and the clean exposure of each detector is about 58.5 ks. RGS 1 and 2 data were not stacked, but were fitted simultaneously in all spectral fits using a cross-calibration constant. The value of this parameter was always close to 1, indicating <5% calibration difference between the two instruments. We binned the RGS spectra by a factor of 3 to achieve only mild oversampling of the instrumental spectral resolution. This was achieved with the "bin" command in the SPEX fitting package (Kaastra et al. 1996). We use the RGS data in the 15 Å (0.83 keV) to 36 Å (0.34 keV) wavelength range. The lower limit is set by the data quality—there is no signal in the RGS data below 15 Å due to the softness of the ASASSN-20qc X-ray spectrum.

To constrain the continuum model, we also examined the EPIC-pn data that extend to higher energies. The EPIC-pn instrument was operated in the Small Window mode. The data were reduced using the EPPROC procedure, and only events of PATTERN ⩽ 4 (single/double) were accepted. We screened for background flares with a threshold of 0.15 counts s^{-1} in the

10–12 keV light curve, keeping in mind the small area of the active CCD during Small Window mode operation. This resulted in a clean exposure time of 35.5 ks. The source region was a circle with a radius of 15″ centered on the ASASSN-20qc position. We specifically chose a small source region size to maximize the signal-to-noise ratio and decrease the background importance at higher energies (>1 keV) considering the extreme softness of ASASSN-20qc. The background region was a polygon on the other side of the pn CCD as the source, at least 150″ away. The source has a count rate of 3 counts s^{-1}, and so pileup should not be an issue during the observation. We confirmed this by assessing the pileup plots produced by the EPATPLOT routine. The data were grouped using the SPECGROUP procedure to at least 25 counts per bin and at the same time to oversample the instrumental resolution by at most a factor of 3. We use EPIC-pn data in the wavelength range between 8 Å (1.55 keV, limited by data quality) and 15 Å (0.83 keV, RGS data available above this limit). We do not use any EPIC-pn data beyond 1.55 keV as the spectrum is strongly background dominated in that range.

We fit the spectra in the SPEX (Kaastra et al. 1996) fitting package. All reduced spectra were converted from OGIP format into SPEX format using the TRAFO routine. We use the Cash statistic (Cash 1979) to analyze the spectra. All uncertainties are provided at 1σ significance.

3. Spectral Modeling and Results

3.1. RGS Analysis

The RGS spectrum of ASASSN-20qc, shown in Figure 1 reveals a plethora of absorption lines which cannot be resolved with EPIC-pn due to its poor spectral resolution below 1 keV. Many of the lines appear highly significant—we particularly note the absorption feature at 26 Å. Most of the lines are narrow, showing widths of the order of a few $100\,\text{s km s}^{-1}$ (FWHM) at most, indicating an ionized absorber with a low velocity width.

We begin the spectral modeling with a baseline continuum fit. The broadband continuum is described with a disk blackbody, the DBB component within SPEX, with a temperature of around 0.18 keV. The definition of the disk blackbody temperature is different in SPEX and XSPEC, resulting in SPEX DBB temperatures being higher by roughly a factor of 2. The disk blackbody is redshifted by $z = 0.056$ using the REDS model. Finally, Galactic absorption is applied using the HOT component. We fix the neutral column density to 1.2×10^{20} cm^{-2} (HI4PI Collaboration et al. 2016). The final fit statistic of the continuum model is C-stat = 1900.68 with 1190 degrees of freedom (DoF).

To determine the absorber properties, we add a PION photoionized absorption component. PION (Miller et al. 2015; Mehdipour et al. 2016) self-consistently calculates absorption line strengths using the ionizing balance determined from the currently loaded spectral continuum model. The ionizing balance is calculated on the fly as the continuum changes during spectral fitting. The PION component allows us to recover the ionized absorber properties such as its column density, ionization parameter $\log(\xi/\text{erg cm s}^{-1})$, outflow velocity, and velocity width. The plasma elemental abundances are fixed to solar values.

The addition of one PION component is highly significant ($\gg 5\sigma$ using the F-test) and improves the fit quality to
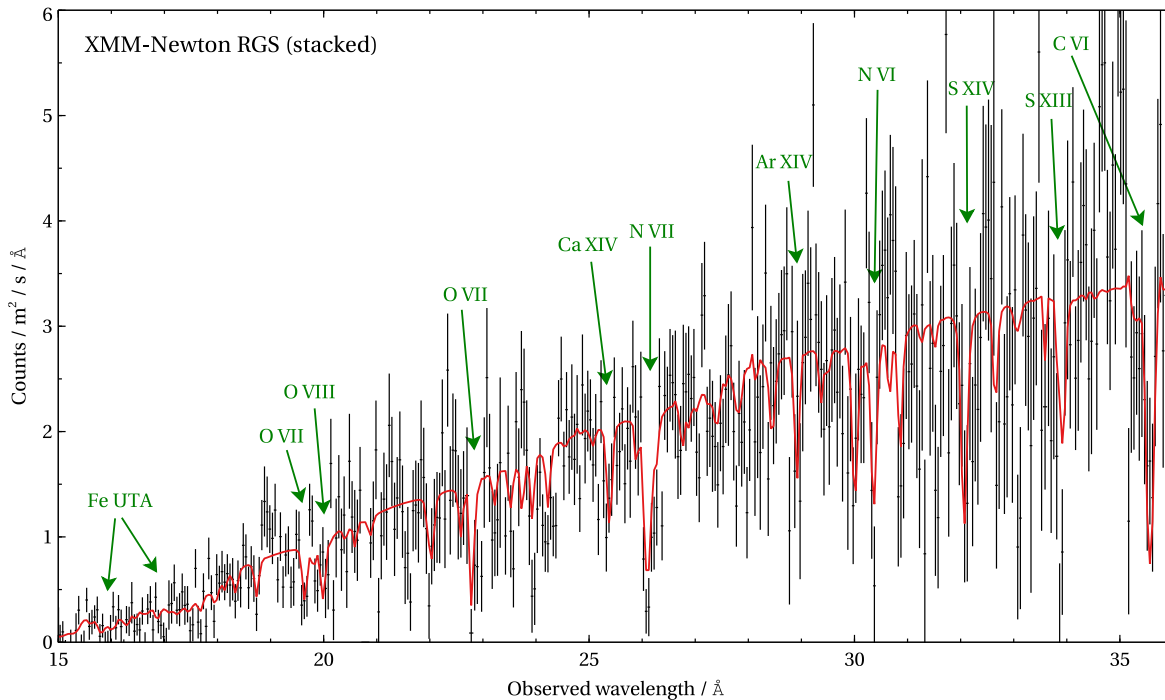
Figure 1. XMM-Newton RGS spectrum of ASASSN-20qc. RGS 1 and RGS 2 spectra are stacked and overbinned for visual purposes only. The best-fitting ionized absorption model, consisting of two photoionized components is shown in red. The most notable elemental transitions are shown with green labels. "Fe UTA" denotes the unresolved transition array of Fe absorption lines.

C-stat = 1748.85 (ΔC-stat = 151.83 over the baseline continuum for four additional DoF). It requires an outflow with a mild velocity of ~800 km s^{-1}, and an ionization parameter $\log(\xi/\mathrm{erg\,cm\,s}^{-1})$ of 3.5. However, many of the absorption lines in the RGS data are still not well fitted in this spectral fit with a single absorber.

This could indicate that a single photoionized absorber is insufficient to fit the observed absorption lines. In other words, the outflow is likely multiphase. To test this hypothesis, we add a second PION component to the previous spectral fit. This step again improves the spectral fit, now to C-stat = 1669.58, a further ΔC-stat = 79.27 over the single phase absorber fit (for four extra DoF), and ΔC-stat = 231.1 over the baseline continuum fit (for eight extra DoF in total). The best-fitting absorber and continuum parameters are listed in Table 1, and the spectral fit is shown in Figure 1. We find one highly ionized absorber with an ionization parameter $\log(\xi/\mathrm{erg\,cm\,s}^{-1})$ of $3.75^{+0.15}_{-0.22}$, and a high column density of $0.25^{+0.14}_{-0.09} \times 10^{24}$ cm^{-2}. The second component is much more mildly ionized at $\log(\xi/\mathrm{erg\,cm\,s}^{-1}) \sim 1.39^{+0.25}_{-0.26}$, and has a much lower column density of $1.5^{+0.4}_{-0.3} \times 10^{21}$ cm^{-2}. Both show low velocity widths, and outflow velocities comparable to those of warm absorbers in regular AGN, but also comparable to the ionized absorber found in the TDE ASASSN-14li (with an outflow velocity of 100–500 km s^{-1}; Miller et al. 2015). The highly ionized component is significantly faster at 910^{+80}_{-90} km s^{-1}, while the second one has a velocity of 380^{+120}_{-100} km s^{-1}.

We note that the column density of the highly ionized absorber is very high (above 10^{23} cm^{-2}), and has significant uncertainties. This value is more than $10\times$ higher than the column density found by Miller et al. (2015) for ASASSN-14li. It is possible that this column density is incorrectly determined from the limited RGS spectrum. Specifically, the spectrum is lacking any information below 15 Å. This spectral region

Table 1
Best-fitting Properties of the Continuum and the Two Ionized Absorbers in the Spectrum of ASASSN-20qc, Determined from an RGS-only Analysis

Component	Parameter	Value
disk	norm	$(320 \pm 40) \times 10^{16}$ m^2
blackbody	kT	$0.197^{+0.004}_{-0.003}$ keV
highly ionized absorber	N_H	$2.5^{+1.4}_{-0.9} \times 10^{23}$ cm^{-2}
	$\log(\xi/\mathrm{erg\,cm\,s}^{-1})$	$3.75^{+0.15}_{-0.22}$
	outflow velocity	910^{+90}_{-80} km s^{-1}
	velocity width	80 ± 20 km s^{-1}
	ΔC-stat	151.83
mildly ionized absorber	N_H	$1.5^{+0.4}_{-0.3} \times 10^{21}$ cm^{-2}
	$\log(\xi/\mathrm{erg\,cm\,s}^{-1})$	$1.39^{+0.25}_{-0.26}$
	outflow velocity	380^{+100}_{-120} km s^{-1}
	velocity width	240^{+70}_{-60} km s^{-1}
	ΔC-stat	79.27

would be important in placing strong upper limits on the outflow column density and the ionization parameter, thanks to the many Fe transitions in the 8–12 Å band. Unfortunately, ASASSN-20qc is spectrally very soft and RGS does not offer sufficient collecting area at higher energies. In the following section, we will use simultaneous EPIC-pn coverage at higher energies (0.8–1.5 keV) to obtain a more reliable measurement of the highly ionized absorber properties.

We further test the properties of the absorbers by freeing their covering fractions (fcov parameter in SPEX). No significant evidence is found for the covering fraction being lower than 1 for any of the two absorbing phases.

We also tried adding a third photoionization phase to the spectral fit. This improves the statistic moderately to

C-stat = 1645.75, a ΔC-stat = 23.83 fit improvement (for four extra DoF) over the previous spectral fit. The best-fitting absorber has a column density of $2.6^{+0.8}_{-0.6} \times 10^{20}$ cm^{-2}, log(ξ /erg cm s^{-1}) of $-1.15^{+0.23}_{-0.17}$, an outflow velocity of 630^{+130}_{-140} km s^{-1}, and a velocity width of 200^{+170}_{-80} km s^{-1}. It improves the spectral fit particularly around 24 Å (Figure 1). The evidence for the third phase indicates that the ionized outflow in ASASSN-20qc is likely highly complex and strongly multiphase. However, only the first two phases strongly modify the high-resolution spectrum and are unambiguously detected at high significance. For this reason, in all our following spectral fits we only include two low-velocity absorber phases.

Finally, we test for the presence of a broad UFO found in the EPIC spectrum (D. Pasham et al. 2023, submitted), in the high-resolution RGS spectra. We take the baseline double slow absorber spectral fit and add a third PION component, now strongly broadened with an FWHM velocity width of about 70,500 km s^{-1} (30,000 km s^{-1} at 1σ, same as used in D Pasham et al., 2023 submitted), outflowing with a large velocity ($<0.1c$). The addition of such a component is not highly significant in the RGS data alone, with a fit statistic C-stat = 1651.90, a ΔC-stat = 17.68 fit improvement. This outcome is not surprising since the residual attributed to the UFO in the EPIC-pn data extends between 0.7 and 1.0 keV. RGS statistics are low in the 0.7–0.8 keV range and data are completely missing above 0.8 keV.

3.2. Simultaneous RGS and EPIC-pn Spectral Modeling

The spectral analysis of the RGS data alone reveals many narrow absorption lines indicating the presence of a low-velocity, multiphase outflow in ASASSN-20qc. At the same time, the RGS results are potentially limited—we are unable to measure the outflow properties reliably due to the lack of RGS data above 0.8 keV. To perform the best possible measurement, we need to combine the RGS and EPIC-pn data sets and fit them simultaneously.

Unfortunately, it is impossible simply to fit these spectra simultaneously over the full energy band. The pn data dominate the fitting statistic, with a count rate $> 10\times$ higher than that of both RGS detectors summed. At the same, the pn data offer a much poorer spectral resolution, and all the individual narrow absorption lines are blended together. Therefore, the fit is driven by broad continuum-like shapes instead of the individual line positions, shapes, and optical depths. This can lead to incorrect results, especially considering that the outflow is multiphase. Furthermore, there are residual calibration differences between the RGS and EPIC-pn instruments, which vary across the overlapping energy band of the instruments (Detmers et al. 2010). These can be important in bright sources such as ASASSN-20qc (with small Poisson error bars on individual EPIC-pn data points) and can systematically skew the best-fitting outflow properties.

A common way to avoid this issue is to ignore the EPIC-pn data in the energy band where RGS has sufficient statistics (around 0.8–0.85 keV in this study), and use a cross-calibration constant to account for any residual calibration uncertainties between the two instruments at the contact energy where the two data sets meet, fitting for the value of this constant. However, this cannot be done in the case of ASASSN-20qc. The EPIC-pn spectrum shows an absorption residual extending from 0.7 to 1.0 keV, i.e., the residual extends across the band where RGS loses statistics, and continues into the EPIC-pn-

only band. Therefore, it is possible that the cross-calibration constant in fact might fit the shape of the absorption residual at the point of contact between the two data sets, instead of the broad instrumental normalization differences. For this reason it is challenging to use the two data sets simultaneously. On the one hand, we do not want to ignore the RGS data below the absorption residual (<0.7 keV), thus losing all the spectral resolution in the important 0.7–0.8 keV region, but on the other hand the unknown cross-calibration difference between the two instruments at the contact point can introduce systematic errors in the spectral fit.

Thankfully, the cross-calibration differences between RGS and EPIC-pn across the energy band are unlikely to be too large, and are at most 15% (Detmers et al. 2010). We can therefore explore the parameter space of these possible differences, to see how much our uncertainty in understanding the instrument cross-calibration affects our outflow modeling and its best-fitting properties. We repeat the same spectral fit for different values of the cross-calibration constant, kept frozen in the range between 0.85 and 1.15, with a step size of 0.05 (seven spectral fits in total for each spectral model).

As mentioned in Section 1, a single blackbody is insufficient to describe the broadband X-ray (0.3–1.5 keV) spectrum of ASASSN-20qc. To improve the description of the continuum, we use two different spectral models describing the combined data set, which have previously been used to fit TDE X-ray spectra.

The first model includes a disk blackbody, two slow absorbers producing the narrow absorption lines, and a fast UFO phase with a large velocity broadening (30,000 km s^{-1} at $1\sigma = 70,500$ km s^{-1} FWHM). This model (blackbody+UFO absorption) model was previously used by Kara et al. (2018) and is also employed to describe the EPIC-pn spectrum of ASASSN-20qc by D. Pasham et al. (2023, submitted). The model represents standard TDE disk blackbody emission from a compact accretion disk, modified by absorption from a high-velocity outflow, launched by the extreme mass accretion rate during the tidal disruption.

We also use an alternative model which does not contain any UFO absorption, and instead applies a continuum consisting of two regular blackbodies, obscured by the two low-velocity absorbers. A disk blackbody and additional warmer continuum has been employed in several recently discovered nuclear transients, including ASASSN-14li (Kara et al. 2018), ASASSN-18el (Ricci et al. 2020; Masterson et al. 2022), and in two TDE candidates later found to also exhibit quasi-periodic eruptions (Miniutti et al. 2019; Chakraborty et al. 2021). This model represents a physical scenario where two different physical components are responsible for the observed spectral continuum. One of these components could be a regular blackbody from an accretion disk, and the second one could originate from shocks, or from Comptonization within a corona. This model is motivated by the broad spectral shape of the UFO model (with a large velocity broadening producing no discrete narrow features), which could in principle be reproduced by a more complex emission continuum spectral shape.
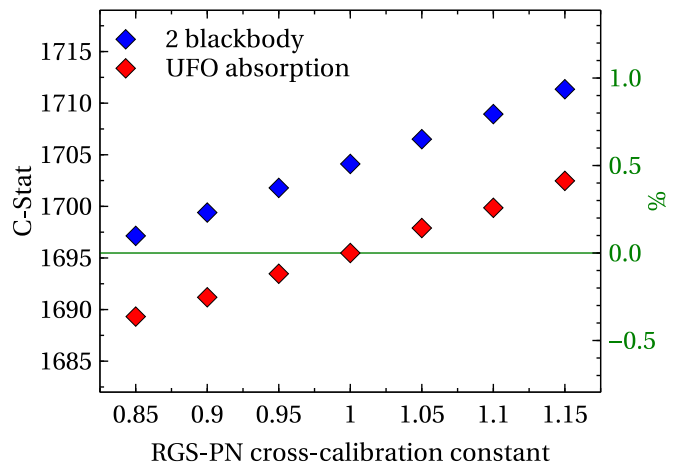
By applying these two different spectral models we are as agnostic as possible to the interpretation of the underlying spectral continuum (which is discussed elsewhere), and show that the determined low-velocity absorber properties are not dependent on this interpretation.
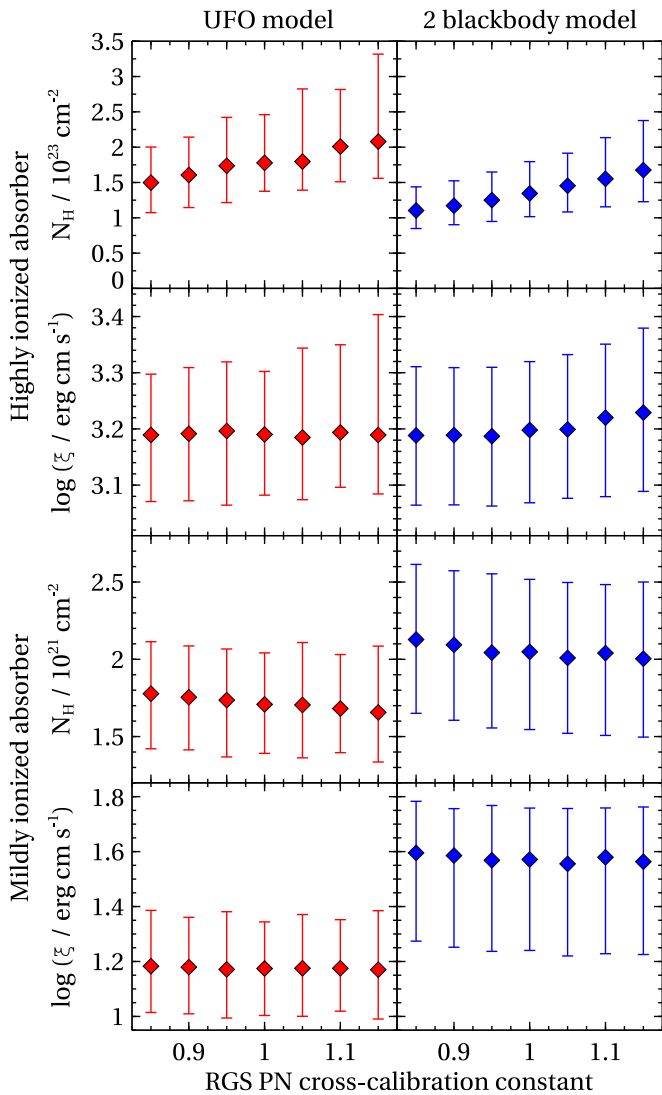
Figure 2. The best-fitting properties of the low-velocity absorbers (assuming photoionization balance) vs. the value of the cross-calibration constant between the RGS and EPIC-pn instruments. The left panels show the results for the UFO model, while the right panels show the double-blackbody model. The top two panels of each column show the column density and ionization parameter for the highly ionized absorber, while the lower two panels show the column density and the ionization parameter for the mildly ionized absorber phase.

Figure 3. The C-stat fit statistic for each model vs. the assumed value of the RGS–EPIC-pn cross-calibration constant. The UFO models are shown in red, while the double-blackbody models are in blue. The right y-axis shows the relative C-stat difference (in %) from the best-fitting UFO model assuming perfect RGS–EPIC-pn cross-calibration.

The absorber properties versus the value of the cross-calibration constant are shown in Figure 2. We find no large steps in the absorber properties over the explored range of cross-calibration constants. All parameters are varying smoothly, with no sudden jumps. Similarly, the fit quality C-stat does not vary significantly with the cross-calibration constant, spanning at most ΔC-stat ~ 15 across the studied range of cross-calibration constant values (Figure 3). In the UFO spectral model, the best-fitting UFO component outflow velocity is around $0.32c$, fully consistent with the results of D. Pasham et al. (2023, submitted). It does not vary significantly with the RGS–EPIC-pn cross-calibration constant. These investigations give us confidence that our results on the properties of the multiphase warm absorber are robust to uncertainties in the continuum model and the cross-calibration constant.

We find that the best-fitting parameters of the highly ionized absorber are consistent between the two spectral models, and do not vary very strongly with the RGS–EPIC-pn cross-calibration constant. Conservatively, we can therefore conclude that the best-fitting highly ionized absorber column density is in the range of $(0.9–3.3) \times 10^{23}$ cm^{-2}, and its ionization parameter $\log(\xi/\mathrm{erg\,cm\,s^{-1}})$ is in the range of 3.0–3.4. We note that these limits are not to be taken at 1σ confidence given the unknown exact value of the cross-calibration between RGS and EPIC-pn. These results, especially the ionization parameter, are somewhat lower than the absorber properties recovered from RGS alone, confirming that RGS overestimates the highly ionized absorber, most likely due to its lack of signal in the important wavelength band below 15 Å. The outflow velocity and the velocity width are consistent with the RGS-only analysis, and does not vary with the RGS–EPIC-pn cross-calibration constant.

We find larger differences between the two models when comparing the mildly ionized absorber. The UFO model results in a somewhat lower column density and ionization parameter. We conclude that the column density of the absorber is most likely in the range of $(1.3–2.6) \times 10^{21}$ cm^{-2}, and its ionization parameter $\log(\xi/\mathrm{erg\,cm\,s^{-1}})$ is in the range of 1.0–1.8. We find that the best-fitting parameters do not vary with the RGS–EPIC-pn cross-calibration constant. The best-fitting outflow velocity and velocity width are again fully consistent with the RGS-only spectral analysis, and do not vary with the cross-calibration constant.

The total C-stat for both spectral models is between 1689 and 1711. The UFO model has 1190 DoF, while the double-blackbody model has 1192 DoF. We find that the UFO model is preferred to the double-blackbody model by about ΔC-stat $\sim$8–9 depending on the exact value of the cross-calibration constant. Simply comparing the difference in DoF and in C-stat values, the UFO model is preferred by our XMM-Newton data by $\sim 2.5\sigma$. However, this simplified comparison does not take into account the great number of DoF in both of these models and is thus only a very rough estimate.

3.3. Time-resolved Spectral Analysis

Miller et al. (2015) found that the ionized absorption in ASASSN-14li is variable on the timescale of a single $\sim$100 ks XMM-Newton observation. The detection of such fast

variability puts strong upper limits on the distance of the ionized outflow from the black hole. Below we investigate whether variability can be detected on single observation timescales in ASASSN-20qc as well. As a first-order approach, we split the XMM-Newton observation into two segments of equal exposure and perform the spectral fit again, tying certain parameters (which are unlikely to vary) together. Given the difficulties discussed above in the spectral model choice and the cross-normalization value when analyzing the RGS and EPIC-pn data together, we perform the outflow variability test for the RGS data alone. Because we are only fitting the RGS data, the parameters recovered for the highly ionized outflow phase might be less trustworthy than in the analysis above, however the variability (in the narrow absorption lines) would be detected nevertheless.

We fit both observation segments simultaneously, employing the two-phase outflow spectral model from Section 3.1. We allow the disk blackbody properties to vary between the segments, as well as the absorber column densities and ionization parameters. We couple the outflow velocities and velocity widths as they are unlikely to change significantly between the two segments, and since we do not visually observe any apparent line shifts between the segments.

The fitting results are shown in Figure 4 and in Table 2. We find that some of the absorber parameters change significantly between the two segments. The largest variation ($>3\sigma$) is surprisingly seen in the mildly ionized absorber ionization parameter $\log(\xi/\mathrm{erg\,cm\,s^{-1}})$, which changes from $1.02^{+0.13}_{-0.12}$ to $1.89^{+0.19}_{-0.20}$ over the course of the 60 ks XMM-Newton observation. We also detect possible variability in the mildly ionized absorber column density ($\sim1.5\sigma$ significance), and in the highly ionized absorber column density ($\sim2\sigma$ significance). Finally, a large difference is also observed in the disk blackbody normalization, however this is necessarily correlated with the apparent variation in the highly ionized absorber column density (the change in continuum absorption is significant as the N_H value is more than 10^{23} cm^{-2} in one of the segments). The observation with the higher highly ionized absorber column density (and greater blackbody luminosity) also shows a slightly greater ionization parameter $\log(\xi/\mathrm{erg\,cm\,s^{-1}})$, however its variation is not statistically significant.

Finally, we consider the variation of the absorber outflow velocities and velocity widths between the two observation segments. We untie all the spectral parameters of the two-phase model and refit. We found that both the outflow velocities and velocity widths of both absorbers are consistent at 1σ confidence between the two segments.

4. Discussion

We study the RGS and EPIC-pn spectra of the TDE ASASSN-20qc and significantly detect a multiphase, low-velocity ionized absorber. Two distinct velocity and ionization components are confirmed, but with further evidence for a third ionization phase, the true nature of this outflow is likely much more complex. The highly ionized phase is faster at 900 km s^{-1}, while the mildly ionized phase is outflowing with a velocity of 400 km s^{-1}. Both of these values are similar to the outflow detected in ASASSN-14li with a velocity of 100–500 km s^{-1} (Miller et al. 2015).

The ionization parameter of the highly ionized phase, $\log(\xi/\mathrm{erg\,cm\,s^{-1}})$ of 3.0−3.4 is comparable with the ionized outflow
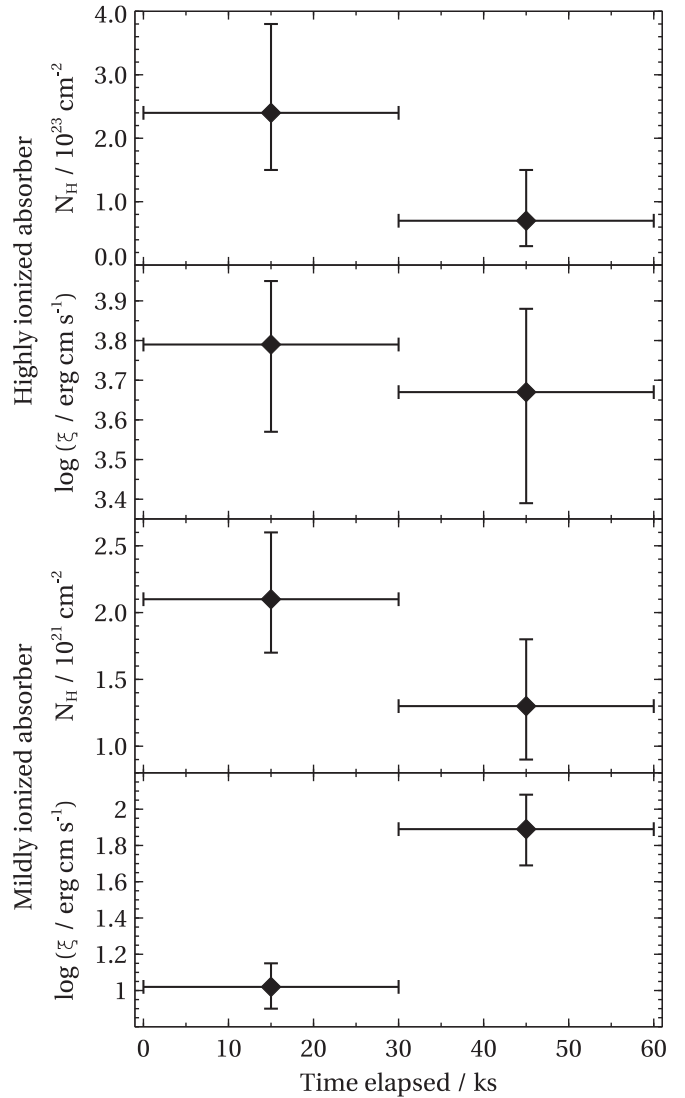
Figure 4. Variation of the best-fitting properties of the low-velocity absorbers during the 60 ks XMM-Newton observation, investigated by splitting it into two segments. The top two panels show the column density and the ionization parameter for the highly ionized absorber phase, while the lower two panels show the column density and the ionization parameter for the mildly ionized phase.

of ASASSN-14li, but it has a much higher column density of $\sim10^{23}$ cm^{-2} versus $(0.5–1.3)\times10^{22}$ cm^{-2} in ASASSN-14li. Such a high column density is surprising, and more similar to the column densities measured in ionized obscurers (e.g., Partington et al. 2023) and UFOs (e.g., Tombesi et al. 2011) in AGN. However, those outflows show much higher systematic velocities than observed in ASASSN-20qc, with obscurers reaching thousands of kilometers per second, and UFOs exceeding $0.05c$. Nevertheless, the absorber of ASASSN-20qc is relatively highly ionized, and so it is still transparent to even soft X-rays, as opposed to obscurers seen in AGN, which tend to absorb most of the source soft X-ray continua.

The mildly ionized absorber phase (alongside with the possible third absorption phase) with an ionization parameter of around 1.5 and a column density of around 10^{21} cm^{-2} is novel and has not been previously detected in TDEs. In its properties, it is very similar to warm absorbers in AGN (Blustin et al. 2005; Laha et al. 2014). The best-fitting time-averaged

Table 2
Time-resolved Analysis of the Ionized Absorption in ASASSN-20qc

Component	Parameter	Segment 1	Segment 2
disk	normalization	$(390 \pm 50) \times 10^{16}$ m^2	$(280 \pm 30) \times 10^{16}$ m^2
blackbody	kT	$0.196^{+0.005}_{-0.004}$ keV	0.194 ± 0.004 keV
highly ionized	N_H	$2.4^{+1.4}_{-0.9} \times 10^{23}$ cm^{-2}	$0.7^{+0.8}_{-0.4} \times 10^{23}$ cm^{-2}
absorber	$\log(\xi/\mathrm{erg\ cm\ s}^{-1})$	$3.79^{+0.16}_{-0.22}$	$3.67^{+0.21}_{-0.28}$
	outflow velocity	910 ± 90 km s^{-1}	
	velocity width	90 ± 20 km s^{-1}	
mildly ionized	N_H	$2.1^{+0.5}_{-0.4} \times 10^{21}$ cm^{-2}	$1.3^{+0.5}_{-0.4} \times 10^{21}$ cm^{-2}
absorber	$\log(\xi/\mathrm{erg\ cm\ s}^{-1})$	$1.02^{+0.13}_{-0.12}$	$1.89^{+0.13}_{-0.20}$
	outflow velocity	410 ± 90 km s^{-1}	
	velocity width	270 ± 50 km s^{-1}	

Note. Best-fitting properties of the continuum and the two ionized absorbers, recovered by fitting the RGS data only. The full XMM-Newton observation was split into two segments with roughly equal exposure.

properties of this phase might suggest that it is a remnant outflow from previous black hole activity, only reilluminated by the current TDE outburst. However, the fast time variability of this component argues against such interpretation.

We can use the best-fitting ionization properties (assuming photoionization equilibrium) of the two phases to estimate their distance from the black hole. Following Kosec et al. (2020), we can use the definition of the ionization parameter $\log(\xi /\mathrm{erg\ cm\ s}^{-1})$ and the definition of the outflow column density N_H to get the following expression for the distance R of the outflow from the ionizing source:

$$R = \frac{L_{ion}}{N_H \xi} \frac{\Delta R}{R}, \qquad (1)$$

where L_{ion} is the 1–1000 Ryd ionizing luminosity and ΔR is the thickness of the absorbing layer. By taking $\frac{\Delta R}{R} = 1$ as the relative thickness of the absorbing layer, which cannot be larger than unity, we can estimate the maximum distance of the absorber from the black hole. The ionization luminosity of ASASSN-20qc, from our X-ray spectral fits, is about 5×10^{44} erg s^{-1}. The maximum distance for the highly ionized phase is thus 2×10^{18} cm $= 0.6$ pc and for the mildly ionized phase is around 1.1×10^{22} cm $= 4000$ pc. We convert these into gravitational radii (R_G) units assuming a black hole mass of 3×10^7 $M_\odot$ (D. Pasham et al. 2023, submitted; we note that Hinkle 2022, estimated a similar black hole mass of 2×10^7 $M_\odot$). For the highly ionized phase, we calculate a maximum distance of 4×10^5 R_G from the black hole, and for the mildly ionized phase we estimate 2×10^9 R_G. These are parsec-scale distances, and serve as an absolute upper limit on the location of the absorbers given their ionization properties. If the absorbers have low relative thicknesses ($\frac{\Delta R}{R} << 1$, i.e., low volume-filling factors), they will be located much closer to the black hole than our estimates.

Instead, we could assume that the outflow velocity of each phase is comparable with the escape velocity at its location. By making this assumption, the distance of the outflow from the black hole is:

$$R = \frac{2GM}{v^2} = 2\frac{c^2}{v^2} R_G, \qquad (2)$$

where R_G is the gravitational radius of the black hole. This assumption results in a distance of $\sim 2 \times 10^5$ R_G (0.4 pc) for the

highly ionized phase, and a distance of $\sim 10^6$ R_G (2 pc) for the mildly ionized absorber phase. The velocity distance estimate is similar to the upper limit from the ionization parameter for the highly ionized component, but wildly different for the mildly ionized component. This result suggests that the mildly ionized component indeed has a very low relative thickness $\frac{\Delta R}{R} < 10^{-3}$, and thus a low volume-filling factor.

Importantly, we also detect significant time variability over the course of the single XMM-Newton observation. Similar variation was previously detected also in ASASSN-14li. Surprisingly, the statistically strongest variation is detected in the mildly ionized absorber properties, rather than in the highly ionized absorber. However, this may be due to the current data set quality, where the variation in the mildly ionized absorber lines is more easily detected than the variation in the highly ionized absorber.

This variation puts an important upper limit on where the outflow can physically reside. If the outflow transverse velocity (with respect to the X-ray source) is too low, it is unable to cross the X-ray source in the limited time (here ~ 30 ks) between the two segments of our observation. Recent results on the size of X-ray emitting regions show that the region is very compact, in most cases with a radius smaller than 10 R_G (Morgan et al. 2008; Dai et al. 2010; Sanfrutos et al. 2013; Chartas et al. 2016). We note that if the emitting region is in fact larger, the resulting distance of the absorber from the black hole is even smaller than the estimate below. Conversely, if the X-ray emitting region is smaller, the absorber can be located farther from the black hole.

For the ASASSN-20qc black hole mass estimate (3×10^7 $M_\odot$), the radius of 10 R_G is 4×10^{13} cm. To cross this radius in 30 ks (or 60 ks for the full diameter) and introduce time variability in the ionized absorption, the absorber needs to move with a transverse velocity of at least 1.5×10^9 cm s^{-1} = 15,000 km s^{-1}. To estimate a rough distance of this absorber from the black hole, we assume that the transverse velocity of the absorber is comparable with the Keplerian velocity at its location. Then its distance from the black hole is roughly:

$$R = \frac{GM}{v^2} = \frac{c^2}{v^2} R_G = 400 \, R_G \qquad (3)$$

.

The time variability puts a much stronger upper bound on the location of the absorber than the ionization balance and the outflow velocity estimates. It indicates that the absorber cannot be a remnant warm absorber from the previous black hole activity, located at parsec scales away from the X-ray source. The outflow hence most likely originates by some launching mechanism from the TDE. Miller et al. (2015) reached a similar conclusion based on the properties of the outflow in ASASSN-14li.

We note that given the black hole mass and the X-ray emitting region size estimates, the outflow has unusual velocity components—a very high toroidal component ($15,000 \text{ km s}^{-1}$) and a very low line-of-sight velocity ($400–900 \text{ km s}^{-1}$). If the assumptions of our calculation hold, our finding likely indicates that the absorber has not reached escape velocity, and is thus not a true outflow. Its kinematic properties (low line-of-sight velocity, high toroidal velocity component) are then more similar to broad line region clouds in regular AGN (Peterson 2006), although the ionization parameter of the absorber in ASASSN-20qc is much higher.

Alternatively, perhaps this suggests that the black hole mass or emitting region size (in R_G) is significantly smaller than we assumed, thus decreasing the necessary transverse velocity requirement and increasing the estimate of the maximum absorber distance from the X-ray source. Given this uncertain estimate of the emitting region size, we caution against using this result as a hard upper bound on the absorber location.

The ionized absorber could be launched directly from the newly formed accretion disk of the TDE. It would probably have to originate in its outer part given the low projected outflow velocity of just a few 100 s km s^{-1}. The launching mechanism is unclear but could be similar to the mechanism powering warm absorbers in regular AGN—possibly radiation line pressure (Proga et al. 2000), magnetic fields (Fukumura et al. 2018), or thermal driving (Waters et al. 2021). Alternatively, the absorber could originate from shocked plasma in the stream–stream collisions of the TDE (Jiang et al. 2016; Lu & Bonnerot 2020). If this is the case, the photoionization calculation based on the assumption of photoionization equilibrium would not hold. However, the important limit on the location inferred from the time variability remains.

At this time, the origin of the ionized absorber remains unknown. Similar absorber detections in further TDEs are needed for a population study to resolve this issue. To our knowledge, ASASSN-20qc is the first TDE to show a multiphase low-velocity outflow in absorption. In particular, the low-ionization component has not been observed elsewhere. We note that Miller et al. (2015) found 3σ evidence for a second, redshifted ionized component in ASASSN-14li, but that component is seen in emission and may form a P-Cygni profile with the primary ionized absorber.

Low-velocity ionized absorbers could be common among the TDE population, but no systematic, sample ionized outflow searches have been published to date. Such studies are challenging due to the data quality of the present high-spectral-resolution TDE observations. Currently, only XMM-Newton and Chandra gratings are capable of performing these studies. ASASSN-20qc ($\sim$8000 source counts) and ASASSN-14li ($>$20,000 source counts) are two of the highest-quality data sets among the small number ($\lesssim$10) of TDEs with usable XMM-Newton or Chandra grating spectra. Long-exposure observations of bright sources, yielding at least a few thousand source counts in the gratings instruments, are necessary to perform a search for ionized outflow signatures.

Low-velocity outflow signatures in TDEs may also be recognized through spectral curvature in lower-resolution CCD spectra, between 0.5 and 1.0 keV. However, it is challenging to confirm this interpretation with CCD-quality data alone. Similar spectral curvature can also be produced by more complex emission continua (double blackbody or blackbody +power law versus a single blackbody), and other spectral features such as high-velocity absorbers (UFOs) in absorption.

New X-ray telescopes, with higher effective area and better spectral resolution in the soft X-ray band ($<$1 keV) are required. Two mission concepts are particularly well suited for observations of soft X-ray TDEs: the proposed X-ray probes Light Element Mapper (LEM; Kraft et al. 2022) and Arcus (Smith 2020). Either one would allow us to study the ionized absorption in TDEs in much greater detail (improved effective area and spectral resolution), and at greater distances (improved effective area), expanding the presently small population of TDEs with X-ray detected ionized absorbers.

5. Conclusions

We analyze XMM-Newton RGS and EPIC-pn spectra of the TDE ASASSN-20qc. The RGS spectrum reveals an array of narrow absorption lines, indicating the presence of an ionized absorber. Our conclusions are as follows:

1. The absorption lines cannot be described by a single photoionization phase, confirming the multiphase nature of this plasma. There are at least two distinct phases: a highly ionized component with a column density of $\sim$$10^{23} \text{ cm}^{-2}$ and a $\log(\xi/\text{erg cm s}^{-1})$ of 3.2, outflowing at 900 km s^{-1}, and a mildly ionized component with a column density of $\sim$$10^{21} \text{ cm}^{-2}$, an ionization parameter of $\sim$1.5, and a velocity of 400 km s^{-1}.
2. The ionized absorption varies in time during the single 60 ks XMM-Newton exposure. The statistically strongest variation is observed in the ionization parameter of the mildly ionized component, but tentative variability is also detected in the highly ionized component.
3. From the best-fitting parameters of the absorbers and their variability, we constrain the location of the ionized absorption to be as low as $\sim$$400 \, R_\mathrm{G}$ from the black hole. Consequently, we cannot be observing a (parsec-scale) remnant outflow launched during previous black hole activity. The origin of the absorbers can be in a disk wind driven from the outer part of the TDE accretion disk, or in the shocked plasma created by stream–stream collisions of the tidally disrupted star.

Software: SPEX (Kaastra et al. 1996), XSPEC (Arnaud 1996), and Veusz.

ORCID iDs

P. Kosec ⓘ https://orcid.org/0000-0003-4511-8427
E. Kara ⓘ https://orcid.org/0000-0003-0172-0854
F. Tombesi ⓘ https://orcid.org/0000-0002-6562-8654

References

Arnaud, K. A. 1996, in ASP Conf. Ser. 101, Astronomical Data Analysis Software and Systems V, ed. G. H. Jacoby & J. Barnes (San Francisco, CA: ASP), 17
Blustin, A. J., Page, M. J., Fuerst, S. V., Branduardi-Raymont, G., & Ashton, C. E. 2005, A&A, 431, 111
Cash, W. 1979, ApJ, 228, 939
Chakraborty, J., Kara, E., Masterson, M., et al. 2021, ApJL, 921, L40
Chartas, G., Rhea, C., Kochanek, C., et al. 2016, AN, 337, 356
Dai, L., McKinney, J. C., Roth, N., Ramirez-Ruiz, E., & Miller, M. C. 2018, ApJL, 859, L20
Dai, X., Kochanek, C. S., Chartas, G., et al. 2010, ApJ, 709, 278
den Herder, J. W., Brinkman, A. C., Kahn, S. M., et al. 2001, A&A, 365, L7
Detmers, R. G., Kaastra, J. S., Costantini, E., et al. 2010, A&A, 516, A61
Fukumura, K., Kazanas, D., Shrader, C., et al. 2018, ApJ, 853, 40
Gezari, S. 2021, ARA&A, 59, 21
Hammerstein, E., van Velzen, S., Gezari, S., et al. 2023, ApJ, 942, 9
HI4PI Collaboration, Ben Bekhti, N., Flöer, L., et al. 2016, A&A, 594, A116
Hinkle, J. T. 2022, arXiv:arXiv:2210.15681
Jansen, F., Lumb, D., Altieri, B., et al. 2001, A&A, 365, L1
Jiang, Y.-F., Guillochon, J., & Loeb, A. 2016, ApJ, 830, 125
Kaastra, J. S., Mewe, R., & Nieuwenhuijzen, H. 1996, UV and X-ray Spectroscopy of Astrophysical and Laboratory Plasmas (Tokyo: Universal Academy Press), 411
Kara, E., Dai, L., Reynolds, C. S., & Kallman, T. 2018, MNRAS, 474, 3593
Kara, E., Miller, J. M., Reynolds, C., & Dai, L. 2016, Natur, 535, 388
Kosec, P., Fabian, A. C., Pinto, C., et al. 2020, MNRAS, 491, 3730
Kosec, P., Pinto, C., Walton, D. J., et al. 2018, MNRAS, 479, 3978
Kraft, R., Markevitch, M., Kilbourne, C., et al. 2022, arXiv:arXiv:2211.09827
Laha, S., Guainazzi, M., Dewangan, G. C., Chakravorty, S., & Kembhavi, A. K. 2014, MNRAS, 441, 2613
Lu, W., & Bonnerot, C. 2020, MNRAS, 492, 686
Masterson, M., Kara, E., Ricci, C., et al. 2022, ApJ, 934, 35
Mehdipour, M., Kaastra, J. S., & Kallman, T. 2016, A&A, 596, A65
Miller, J. M., Kaastra, J. S., Miller, M. C., et al. 2015, Natur, 526, 542
Miniutti, G., Saxton, R. D., Giustini, M., et al. 2019, Natur, 573, 381
Morgan, C. W., Kochanek, C. S., Dai, X., Morgan, N. D., & Falco, E. E. 2008, ApJ, 689, 755
Nicholl, M., Wevers, T., Oates, S. R., et al. 2020, MNRAS, 499, 482
Ohsuga, K., & Mineshige, S. 2011, ApJ, 736, 2
Ohsuga, K., Mineshige, S., Mori, M., & Kato, Y. 2009, PASJ, 61, L7
Ohsuga, K., Mori, M., Nakamoto, T., & Mineshige, S. 2005, ApJ, 628, 368
Partington, E. R., Cackett, E. M., Kara, E., et al. 2023, ApJ, 947, 2
Peterson, B. M. 2006, in Physics of Active Galactic Nuclei at all Scales, ed. D. Alloin, Vol. 693 (Berlin: Springer), 77
Pinto, C., Middleton, M. J., & Fabian, A. C. 2016, Natur, 533, 64
Pinto, C., Soria, R., Walton, D. J., et al. 2021, MNRAS, 505, 5058
Pounds, K. A., Reeves, J. N., King, A. R., et al. 2003, MNRAS, 345, 705
Proga, D., Stone, J. M., & Kallman, T. R. 2000, ApJ, 543, 686
Rees, M. J. 1988, Natur, 333, 523
Ricci, C., Kara, E., Loewenstein, M., et al. 2020, ApJL, 898, L1
Sanfrutos, M., Miniutti, G., Agís-González, B., et al. 2013, MNRAS, 436, 1588
Saxton, R., Komossa, S., Auchettl, K., & Jonker, P. G. 2020, SSRv, 216, 85
Sazonov, S., Gilfanov, M., Medvedev, P., et al. 2021, MNRAS, 508, 3820
Shakura, N. I., & Sunyaev, R. A. 1973, A&A, 24, 337
Smith, R. K. 2020, Proc. SPIE, 11444, 114442C
Stanek, K. Z. 2020, TNSTR, 2020-3850, 1
Strüder, L., Briel, U., Dennerl, K., et al. 2001, A&A, 365, L18
Takeuchi, S., Ohsuga, K., & Mineshige, S. 2013, PASJ, 65, 88
Tombesi, F., Cappi, M., Reeves, J. N., et al. 2011, ApJ, 742, 44
Tombesi, F., Cappi, M., Reeves, J. N., et al. 2010, A&A, 521, A57
van Velzen, S., Gezari, S., Hammerstein, E., et al. 2021, ApJ, 908, 4
Waters, T., Proga, D., & Dannen, R. 2021, ApJ, 914, 62